Journal of Theoretical and Applied Information Technology
31st August 2026. Vol.104. No.16

ISSN: 1992-8645 www.jatit.org E-ISSN: 1817-3195

ADAPTIVE FROST-FILTERED DEEP FEATURE FUSION WITH METAHEURISTIC-OPTIMIZED WGAN-AUTOENCODER FOR IOT-ASSISTED SKIN CANCER DETECTION

MUTHAMIZHAN M[1], B SATHYASRI[2]

[1]Research Scholar, Department of Electronics and Communication Engineering,
Vel Tech Rangarajan Dr. Sagunthala R & D Institute of Science and Technology, Chennai, India

[2]Professor, Department of Electronics and Communication Engineering,
Vel Tech Rangarajan Dr. Sagunthala R & D Institute of Science and Technology, Chennai, India

E-mail: muthamizhan2770@gmail.com, sathyasrib@veltech.edu.in

ABSTRACT

Internet of Things (IoT) aided skin cancer detection incorporates many linked sensors and devices to support the main study and observation of skin modalities. Skin cancer is measured as one of the hazardous types of cancer and there is a severe upsurge in the number of deaths owing to a low level of awareness of the signs and their prevention. Therefore, early identification at a primary phase is essential so that one can avoid the increase of cancer. Recently, IoT-based skin cancer detection using deep learning (DL) was employed for improving the prompt analysis and observation of skin cancer. This paper presents a Hybrid Deep Learning and Feature Extraction Technique for Enhanced Skin Cancer Diagnosis through Medical Imaging (HDLFET-ESCDMI) model. The aim of the paper is to develop an IoT-assisted medical image analysis framework for accurate skin cancer diagnosis using advanced techniques. Initially, the image pre-processing stage employs an extended-tuned adaptive frost filtering (Ext-AFF) technique for eliminating the noise to enhance image quality. Besides, the extraction of the feature process has been executed by the ConvNeXt-X model to recognize and isolate the most significant information from raw data. For the classification procedure, the presented HDLFET-ESCDMI model implements a hybrid Wasserstein generative adversarial network and autoencoder (WGAN-AE) technique. At last, the red-billed blue magpie algorithm (RBMO)-based parameter fine-tuning procedure is implemented to enhance the classification outcomes of the WGAN-AE system. A comprehensive experiment was implemented to verify the performance of the HDLFET-ESCDMI. The performance results designated that the HDLFET-ESCDMI underscored advancement over other recent techniques.

Keywords: *Hybrid Deep Learning, Feature Extraction, Skin Cancer Diagnosis, Medical Imaging, Internet of Things, Hyperparameter Tuning*

1. INTRODUCTION

The Internet of Things (IoT) is created by connecting tools to the Internet through modern communication technologies for sharing data [1]. Currently, IoT is increasingly applied in numerous applications, including smart grids, smart cities, smart homes, body sensor networks, and vehicular ad hoc networks. The growth of IoT relies on various sophisticated techniques, such as information sensing, cloud computing (CC), and wireless sensor networks (WSNs). IoT is frequently used to improve and create healthcare systems because of its efficient ability to integrate with infrastructure resources and provide vital information to users [2]. The medical care systems provide a significant amount of information over WSN after allocating several e-health services, such as medical platforms, remote patient monitoring, and electronic health records. In general, skin comprises cells, and those cells contain tissues [3]. Therefore, cancer is triggered because of irregular or uncontrolled cell propagation in the same tissues or other nearby tissues. Contact with UV rays, family history, a weakened immune system, etc., might be the cause of the existence of cancer. Benign tumors are a type of noncancerous growth and are usually referred to as moles, which aren't dangerous [4]. In contrast, malignant tumors are considered cancerous and pose a threat to life [5].

Among them, Melanoma is the most severe and can reappear even after being removed. For improved outcomes, initial diagnosis of skin cancer is vital, although identifying solid tumors generally depends upon screening mammography with limited sensitivity, which is later confirmed by clinical samples [6]. Numerous healthcare professionals are utilizing artificial intelligence (AI) to support and improve the diagnosis decision-making process.

Computer-aided design (CAD) can rapidly, consistently, and reliably diagnose several diseases [7]. CAD also gives the choice for sophisticated cancer detection and prevention, which is accurate and affordable. Human organ disorders are normally examined by numerous imaging techniques. Computed tomography (CT) is a clinical screening tool, dermatoscopy image analysis, and other techniques that are primarily utilized for visually diagnosing skin lesions [8]. Dermatologists with little knowledge have displayed decreased precision in skin lesion diagnostics. The techniques doctors use to assess and examine lesion images are complex, a longer process, imperfect, and subjective [9]. Deep learning (DL) has transformed the complete environment of machine learning (ML) recently. It is recognized as the advanced ML sub-branch involved in artificial neural network (ANN) models. Such models are influenced by the human brain's function and structure. DL methods are applied in several fields. When compared to other conventional methodologies, ML and DL techniques have attained extraordinary outcomes in these applications [10].

This study presents a Hybrid Deep Learning and Feature Extraction Technique for Enhanced Skin Cancer Diagnosis through Medical Imaging (HDLFET-ESCDMI) model. Initially, the image pre-processing stage employs an extended-tuned adaptive frost filtering (Ext-AFF) approach for eliminating the noise to enhance image quality. Besides, the extraction of the feature process has been executed by the ConvNeXt-X model to recognize and isolate the most significant information from raw data. For the process of classification, the presented HDLFET-ESCDMI model implements a hybrid Wasserstein generative adversarial network and autoencoder (WGAN-AE) technique. At last, the red-billed blue magpie algorithm (RBMO)–based parameter fine-tuning method is implemented to enhance the classification outcomes of the WGAN-AE system. The performance outcomes specified that the HDLFET-ESCDMI approach underscored improvement over other existing techniques.

1.1 Problem Statement and Research Questions

Manual dermoscopic evaluation of skin lesions remains time-consuming, subjective, and heavily dependent on dermatologist expertise, which contributes to delayed diagnosis and inconsistent accuracy, particularly in resource-constrained and remote settings. Existing IoT- and deep-learning-based computer-aided diagnosis (CAD) systems are further limited by noise-sensitive pre-processing, suboptimal feature extraction from heterogeneous dermoscopic images, sensitivity to class imbalance across lesion types, and manually tuned hyperparameters that hinder reproducibility and scalability. This study addresses these limitations by designing an integrated IoT-assisted diagnostic pipeline. The specific research questions (RQs) guiding this work are:

RQ1: How can adaptive frost-filtering be tuned to suppress speckle noise in IoT-acquired dermoscopic images while preserving diagnostically relevant edge and texture detail?

RQ2: Can a hybrid CNN-Transformer feature extractor (ConvNeXt-X) yield more discriminative representations for multi-class skin lesion classification than conventional CNN backbones?

RQ3: Does a hybrid Wasserstein GAN-Autoencoder (WGAN-AE) classifier improve robustness and generalization over standalone discriminative classifiers, particularly for minority lesion classes such as Dermatofibroma and Seborrheic Keratosis?

RQ4: Can a bio-inspired metaheuristic (the Red-Billed Blue Magpie Optimizer) automate hyperparameter selection to improve classification accuracy while reducing the computational time overhead relevant to IoT deployment?

2. REVIEW OF LITERATURE WORKS

Sara et al. [11] incorporated a Skin Lesion Cancer feature extractor CNN (SLC-CNN) approach. In this approach, test images of skin lesions are captured and preprocessed for classification as well as segmentation processes. After preprocessing, the testing image features are removed by the feature representation of the SLC-CNN, whose features are utilized in SVM for classifying skin cancer types, and with the classification outcome, the XGBoost

method is used for segmenting the cancer area. Akinrinade and Du [12] presented a new methodology that uses unprocessed images to train and test images for testing data. Then, those input images are preprocessed through the deeper model for identifying and predicting the following outputs. Furthermore, CNN's impact on forecasting precision employing a texture of the skin lesion to distinguish between cancerous as well as non-cancerous lesions is also analyzed through recovered image fundamentals from skin images that are important to identify skin cancer. Kaur et al. [13] focused on developing effective methods for numerous stages of melanoma CAD. The CAD's foremost stage encompasses the suggested hybrid technique that utilizes morphologic operation and context aggregation-based DNN for removing hairlines and improving low dissimilarity in dermoscopic skin lesion images.

The authors [14] introduced a new technique to precisely identify skin cancer through a CNN model and hyperparameter optimization. This model intends to raise the correctness and effectiveness of skin cancer diagnosis and thus improve the experience of the patient. Akilandasowmya et al. [15] exploited the sand cat swarm optimizer alongside the ResNet-50 (SCSO-ResNet50) for deep unknown feature separation from known features, guaranteeing precise estimations. The authors deploy an improved harmony search (EHS) algorithm to augment features and minimize data reduction. It manages practical data streaming, prediction, and dimensionality problems.

Asiri et al. [16] aimed to develop Smart IoT alongside a DL-driven Skin Lesion Diagnosis (IIoT-DLSLD) approach for the medical domain. This approach allows IoT systems to extract dermoscopic images and categorize skin cancers into different classes. Moreover, this approach leverages the Gaussian filtering (GF) pre-processing technique for noise removal. Reddy et al. [17] presented a Bi-LSTM architecture for detecting skin cancer. The African Vulture Optimizer Algorithm (AVOA) has been developed for selecting optimal skin image features. In this study, this issue is resolved by utilizing a GAN to produce additional training images. Classical RNNs are focused on rectifying memory limitations. In [18], a novel scheme for SCD utilizing an optimizer approach and ANN is suggested. Image segmentation to identify the lesion region is executed through a Kohonen neural network, in which the recognized ROI is improved by the Greedy Search Algorithm (GSA).

Despite these advances, several gaps persist. Sara et al. [11] and Akinrinade and Du [12] rely on standard CNN pipelines without adaptive noise suppression, so classification accuracy degrades on noisy, IoT-acquired dermoscopic images. Asiri et al. [16] apply Gaussian filtering, which removes noise uniformly but blurs lesion boundaries that are diagnostically significant. Reddy et al. [17] employ Bi-LSTM architectures, which, despite GAN-based augmentation, remain constrained by the sequential-memory limitations inherent to RNN-based models when applied to high-dimensional image data. Moreover, most reviewed approaches [11–18] tune hyperparameters manually or through grid search, which is computationally expensive and does not guarantee optimal configurations. This gap in noise-robust pre-processing, transformer-aware feature extraction, generative-discriminative hybrid classification, and automated hyperparameter optimization for IoT-based skin cancer diagnosis motivates the proposed HDLFET-ESCDMI framework, which integrates Ext-AFF, ConvNeXt-X, WGAN-AE, and RBMO into a single, systematically validated pipeline.

3. PROPOSED METHODOLOGY

In this article, we have presented an innovative HDLFET-ESCDMI model. The paper aims to develop an IoT-assisted medical image analysis framework for accurate skin cancer diagnosis using advanced techniques. It contains four distinct kinds of processes image preprocessing, feature representation model, hybrid classification process, and parameter fine-tuned. Fig. 1 depicts the overall flow of the HDLFET-ESCDMI model.

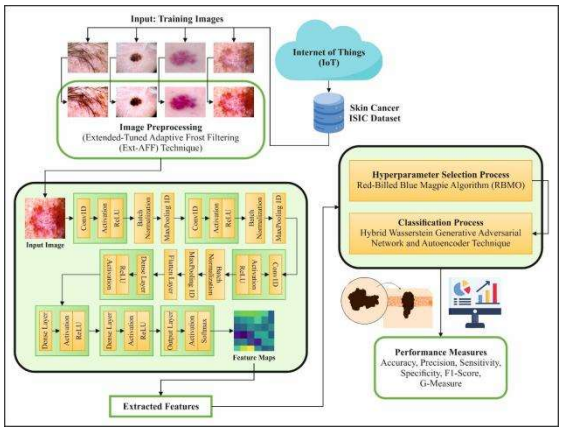

Figure 1: Overall flow of HDLFET-ESCDMI Technique

3.1. Image Pre-processing

Initially, the image pre-processing stage employs the Ext-AFF technique to eliminate the noise to enhance image quality. The raw images gathered from the dataset show a higher level of noise than the image analysis's efficacy [19]. Conventional frosting-filtering models minimize surplus speckle noise normally negotiating the architectural details of the images. The presented architecture deals with this restriction by using an Ext-AFF model, while all pixels are adjusted with values to improve the image quality while maintaining significant architectural information. This model characterizes an expansion of the normal frost filters inside the Lee and Kuan filters over the feature of adaptive tuning, effectively improving trade-off efficacy among noise reduction and edge detail retention. To improve the generalization and robustness of the presented architecture through changing image qualities, complete data pre-processing is used. Pre-processing takes advantage of Ext-AFF to increase the quality of the image by successfully minimizing noise while maintaining important edge information. This stage was vital to guaranteeing constant feature extraction, particularly specifying the variabilities in image resolutions and levels of noise through the database. It is represented mathematically by Eq. (1) as demonstrated,

$$\hat{Z}(u,v)_{=}\sum_{a}\sum_{b}P_{ab}\,m_{ab}/\sum_{a}\sum_{b}m_{ab},k_{ab}=\exp\left(-QC_{Z}^{2}d_{ab}\right) \quad (1)$$

Here, (u, v) specifies that the current pixel position, $\hat{Z}(u, v)$ designates the filter result, characterizes the values of pixels amongst the center window at (u, v), Q $(Q > 0)$ point out the tuning factor (TF), C_Z displays the coefficient of variation that represents the ratio of the sample mean to the standard deviation (SD), and d_{xy} embodies the distance between the center and current pixels.

During the presented filter system, in TF, Q can be extremely significant in boosting the performance of the Ext-AFF approach. If Q value is lower, it overcomes noise however failed to maintain the important data and edge pixels. If the Q value is higher, the noises are suppressed then the edge pixel preservation becomes enhanced. Besides, t-estimation is applied to characterize the center pixel owing to the sample variance and the mean is standardized through complete pixels in the presented window.

$$Q(a,b)=T(t_0)\times U(a,b) \quad (2)$$

$$T(t_0)=\frac{/Z(t_0)-m(t_0)/}{\lambda(t_0)} \quad (3)$$

$$Q(a,b)=\frac{/Z(a,b)-Z(t_0)/}{\frac{1}{(2L+1)^2-1}\sum_{m=u-L}^{u+L}\sum_{n=p-L}^{v+L}|Z(m,n)-Z(t_0)|} \quad (4)$$

N, $Q(a, b)$ is the extended factor of tuned adjusted according to t-evaluation $T(t_0)$, $U(a, b)$ specifies the adjacent pixels of the grayscale, $Z(t_0)$ epitomizes the value of the center pixel. Also, $\lambda(t_0)$ and $m(t_0)$ embody the present mean of the center window, and the SD of pixels at t_0 and L specify the window size. The presented model can create higher-quality images with conserved important architectural features that are significant for the final steps of analysis.

3.2. ConvNeXt-X Model

Besides, the extraction of the feature process has been executed by the ConvNeXt-X model to recognize and isolate the most significant information from raw data. ConvNeXt is a new CNN structure tailored for improving performance by incorporating the powers of classic convolution networks with novelties from transformer methods [20]. It arrives at different alternatives, comprising ConvNeXtBase, ConvNeXtTiny, and ConvNeXtSmall, which provide dissimilar computational requirements and use cases. Its key aim is to supply greater scalability and performance, preserving the easiness of conventional CNNs while combining main inventions from vision transformers (ViTs). It is a progressive DL structure, which improves traditional convolutional neural networks (CNNs) by presenting numerous main changes to increase performance, generalization, and efficiency. The succeeding sections offer comprehensive data about the structure of ConvNeXt, comprising its main elements, methods, and main characteristics:

ConvNeXt continues traditional CNNs by combining various innovative methodologies, comprising:

- **Depth-wise Convolutions:** It uses one filter for all input channels individually, as different from the normal convolution, which combines every channel. Depth-wise convolutions lower the parameter counts and computational usage, making

the method more effective but preserving performance.

- **Residual Connections:** It permits the method to skip the above layers, aiding to contest the problem of gradient vanishing and encouraging the improved flow of information during the network.
- **Global Average Pooling (GAP):** It substitutes the layers of fully connected (FC) normally discovered in CNNs. This approach reduces the model's complexity and aids in alleviating overfitting.
- **Batch Normalization (BN):** It standardizes the resultant of all layers to have a mean of 0 and an SD of 1, enhancing stability and training speed.
- **Non-Linear Activation Functions:** It utilizes activation functions such as Gaussian Error Linear Units (GELU) or ReLU to present nonlinearity, permitting the method for learning more composite patterns.

These structural changes permit ConvNeXt to provide either higher performance or computational effectiveness through dissimilar use cases. It provided different versions, each tailored for dissimilar use cases and computational resources. The 3 major versions are:

- **ConvNeXtTiny:** It is a smaller and lightweight form of ConvNeXt, specially intended for use cases while computing capacity is restricted or a real-time process is needed. It reduces the parameter counts and lowers computing power, making it appropriate for mobile applications and edge devices. Despite its compact dimension, it preserves the main structural modules.
- **ConvNeXtSmall:** Positioned among ConvNeXtBase and ConvNeXtTiny, this version provides a balanced trade-off between computing cost and performance. It comprises additional parameters and layers than the small version, making it appropriate for more challenging applications, while either precision or effective calculation is important. ConvNeXtSmall advantages from MHSA mechanisms and progressive convolution layers, allowing it to apprehend either global or local features more successfully.
- **ConvNeXtBase:** It is tailored for higher-performance calculating environments and is the most powerful form in the ConvNeXt family. It contains larger parameter counts and deep layers, which makes it best for tasks demanding wide-ranging precision and capacity of the model, namely object detection, segmentation, and high-resolution image classification. It combines progressive methods such as GELU activation functions and patchy stem to improve feature extractor while preserving computational complexity.

The ConvNeXt structure combines many major operations that are characterized mathematically as shown:

• Depth-wise Convolutions:

$$y=\sum_{i=1}^{C} x_i * w_i \quad (5)$$

Whereas x_i embodies the input feature mapping for channel i, w_i embodies the filter for channel i, and the amount is removed from each input channel.

• Residual Connections:

$$y=F(x)+x \quad (6)$$

Here, $F(x)$ denotes the resultant from the convolution layer, and x means input to layer.

• GAP:

$$GAP(x)=\frac{1}{H\times W}\sum_{i=1}^{H}\sum_{j=1}^{W} x_{ij} \quad (7)$$

Now, H and W imply the width and height of input feature mapping, and x_{ij} characterizes the value at location (i, j) within the feature mapping.

• BN:

$$\hat{x}=\frac{x-\mu}{\sqrt{\sigma^2+e}} \quad (8)$$

Here, σ^2 and μ represent the variance and mean of the batch, ε means a smaller constant to prevent division by 0, and x refers to input to the BN layer.

• Activation Functions (GELU):

$$GELU(x)=0.5x\left(1+\tanh\left(\sqrt{\frac{2}{\pi}}(x+0.044715x^3)\right)\right) \quad (9)$$

GELU is a smoother nonlinear function of the activation that is exposed to implement well in deeper networks in comparison with ReLU, particularly in tasks needing accurate feature extraction.

3.3. Hybrid WGAN-AE Technique

For the classification process, the proposed HDLFET-ESCDMI model implements a hybrid WGAN-AE technique. It is an advanced technique, which incorporates the top features of AEs with GANs to provide better performances [21]. This method has dual major components: Discriminator and AE. Besides that, the loss of Wasserstein aids increases the stabilities of the training as the complete method is learned to rebuild the input data and differentiate between actual and what is imitated. This method is mathematically expressed in the following section.

The AE learns to precisely input/compress data into lower-dimensional representations, capable of reconstructing similar input data from lower-dimensional areas.

- **Encoder:** It maps the input data xi from the input area $\mathbb{R}^d$ to the low-dimension latent area. It is described by the function $f_\theta : \mathbb{R}^d \rightarrow \mathbb{R}^z$, while θ signifies the encoding parameters, and $z \in \mathbb{R}^z$ denotes the latent model.

$$z_i=f_\theta(x_i) \quad (10)$$

Whereas, z_i refers to compressed representations of x_i.

- **Decoder:** It has the responsibility to reconstruct the new input x_i from the latent vector z_i. The decoding function of $g\phi : \mathbb{R}^z \rightarrow \mathbb{R}^d$ was parameterized by ϕ, and the reconstruction $\hat{x}_i$ is provided by:

$$\hat{x}_i=g_\phi(z_i) \quad (11)$$

Here, $\hat{x}_i$ refers to reconstructed input.

The AE's loss function is normally the loss of reconstruction that estimates how much the decoding may estimate the new input xi from latent codes z_i.

$$L_{recon}(x_i,\hat{x}_i)=\|x_i-\hat{x}_i\|_2^2 \quad (12)$$

Whereas, $\|\cdot\|_2$ signifies the squared Euclidean distance.

For the input data x_i, the discriminator outputs the scalar $D_\psi(x_i)$ demonstrating the likelihood that x_i is real. Thus, the discriminator loss is designated as in Eq. (13):

$$L_{disc}(x_i,\hat{x}_i)=-E_{x\sim P_{real}}[\log D_\psi(x)]-E_{\hat{x}\sim P_{gen}}\left[\log\left(1-D_\psi(\hat{x})\right)\right] \quad (13)$$

Here, P_{real} specifies the distribution of actual data and P_{gen} embodies the produced data distribution. The discriminator aims to accurately categorize fake data as zero and real data as one, reducing the above-mentioned function of loss.

$$L_{Wasserstein}(x_i,\hat{x}_i)=E_{x\sim P_{real}}[D_\psi(x)]-E_{\hat{x}\sim P_{gen}}[D_\psi(\hat{x})] \quad (14)$$

This loss function trains the discriminator to provide higher values to actual data and lower values to the created data, therefore making an attempt to improve the distance among the dual distributions. It has smooth gradients and resolves the problem of gradient vanishing which is standard for typical GANs. It is trained to reduce the loss of Wasserstein in the opposed path.

During this technique, the incorporated technique is trained together with either the discriminator or the generator. However, the generator attempts to reduce the error of reconstruction also such that the created data is either consistent or realistic using the input data.

$$L_{combined}=\lambda_{recon}L_{recon}(x_i,\hat{x}_i)+\lambda_{Wasserstein}L_{Wasserstein}(x_i,\hat{x}_i) \quad (15)$$

Here, $\lambda_{Wasserstein}$ and λ_{recon} denote hyper parameters that control the relative significance of the Wasserstein and the reconstruction losses.

3.4. Parameter Tuning using RBMO Algorithm

Eventually, the RBMO-based parameter selection model is implemented to increase the classification outcomes of the WGAN-AE system. The red-billed blue magpies are well-known for their larger physique and their feeding tactics are flexible and consist of walking on the ground, weaving, and jumping between branches, particularly in the morning hours and at sunset [22]. Their social communications are highly influential after searching together. After they discover food, like insects or fruits, they immediately signal to gather their companion and cooperate to collect the target. This suggested cooperation permits them to simply advance their defenses of the prey. Additionally, they further reveal individual storage behavior and hide their food in unseen locations like tree holes,

and gaps between rock crevices or branches to escape being caught by another predator. It is the individual environmental feature, which offers a richer source of ideas for the model of the RBMO meta-heuristic model.

Initialization phase: The RBM's population is initially generated at random. Assume that N RBMs are in the D-dimensional area, with every RBM positioned as a matrix x of size $N \times D$ as shown in Eq. (16),

$$x=\begin{bmatrix} x_{1,1} & x_{1,2} & \cdots & x_{1,j} & \cdots & x_{1,D} \\ x_{2,1} & x_{2,2} & \cdots & x_{2,j} & \cdots & x_{2,D} \\ \vdots & \vdots & \ddots & \vdots & \ddots & \vdots \\ x_{i,1} & x_{i,2} & \cdots & x_{i,j} & \cdots & x_{i,D} \\ \vdots & \vdots & \ddots & \vdots & \ddots & \vdots \\ x_{N,1} & x_{N,2} & \cdots & x_{N,j} & \cdots & x_{N,D} \end{bmatrix}_{N\times D} \quad (16)$$

Whereas, $i = 1, 2, \ldots, N, j = 1, 2, \ldots, D$, X_i^j signifies the location of the *ith* RBM in size j. N refers to RBM's population size and D problem dimension.

Search behavior: They naturally forage in smaller groups that facilitate a more effective search and improved survival of the population. They look for food on the ground or in the forest by flying and hopping. This flexibility allows RBM to accept different hunting tactics according to environmental features and resource accessibility, guaranteeing a stable supply of food. If groups gather to hunt, the mathematical representation is as shown:

$$x_{i+1}=X_i+rand1\times\left(\frac{1}{n}\times\sum_{k}^{n}X_k-X_{rs}\right) \quad (17)$$

Whereas X_i characterizes the *ith* individual, n signifies the RBM's group counts chosen at random from the search population, varying from 2 to 5, X_k denotes the *kth* individual selected at random, and X_{rs} characterizes the search agent selected randomly in the present iteration.

$$X_{i+1}=X_i+rand2\times\left(\frac{1}{m}\times\sum_{k}^{m}X_k-X_{rs}\right) \quad (18)$$

Here, m characterizes the search agent counts in the group looking for food. The search agent counts are chosen at random from the complete population.

Preying behavior: RBM determines outstanding hunting skills and teamwork, mainly after searching for prey. They utilize a range of strategies, comprising jumping, fast pecking, and flying traps of insects. Individually or in smaller groups, they have a habit of hunting smaller targets and collecting plants, a procedure that is defined by Eq. (19). Once grouped, they can attack large targets like larger insects and smaller vertebrates in a coherent way, and this cooperative predatory behavior is represented in Eq. (20).

$$X_{i+1}=X_{food}+CF\times rand1\times\left(\frac{1}{n}\times\sum_{k}^{n}X_k-X_{rs}\right) \quad (19)$$

$$X_{i+1}=X_{food}+CF\times rand2\times\left(\frac{1}{m}\times\sum_{k}^{m}X_k-X_{rs}\right) \quad (20)$$

Whereas, X_{food} characterizes the food location, $CF = (1 - (t/T))^{(2t/T)}$, represents a factor of conditioning, and rand symbolizes a value preferred at random in the interval of [0, 1].

Storage behavior: If RBMs hunt excess food, they warehouse it in an unseen location or tree hole for the winter season food scarcity. This procedure is expressed as maintaining the best solution to more successfully recognize the global optimal.

$$X_{i+1}=\begin{cases}X_i & if\ fitness_{old}>fitness_{new}\\ X_{i+1} & else\end{cases} \quad (21)$$

Whereas, $fitness_{old}$ and $fitness_{new}$ symbolize the fitness values of the RBM following location upgrades, correspondingly. The pseudo-code for RBMO is specified in Algorithm 1. Fig. 2 illustrates the flowchart of the RBMO algorithm.

Algorithm 1: Pseudo Code of RBMO

```
Set Problem Setting (D, lb, ub, N, T_max, t)
Set the solution places arbitrarily
Compute the fitness function (FF)
Discover the optimal place
While t<T_max do
 For i<N
        Search Behavior
                if rand<p
                        Utilizing Eq. (17)
                else
                        Utilizing Eq. (18)
        Predator behavior
                if rand<p
                        Utilizing Eq. (19)
                else
                        Utilizing Eq. (20)
                Storage Behavior
                        Utilizing Eq. (21)
 end
 Upgrade the best Red-billed blue magpie
end
Return optimal solution
```

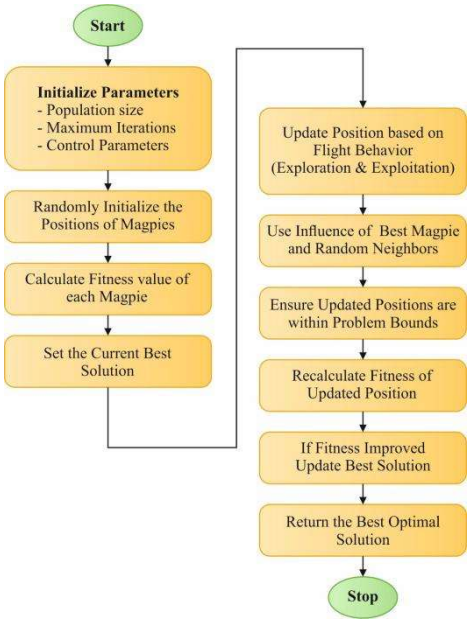

Figure 2: Flowchart of RBMO

The RBMO system creates an FF to achieve improved classifier performance. It explains a progressive number to indicate the heightened effectiveness of candidate solution. The reduction of the classifier rate of error is determined as FF.

$$fitness(x_i) = ClassifierErrorRate(x_i)$$

$$= \frac{no\ of\ misclassified\ samples}{Total\ no\ of\ samples} * 100 \quad (22)$$

4. PERFORMANCE VALIDATION

The performance evaluation of HDLFET-ESCDMI model is examined under Skin cancer ISIC database [23]. This database comprises 2239images under nine diseases as depicted in Table 1. Fig. 3 demonstrates the sample images.Fig. 4 depicts the classifier outcomes of the HDLFET-ESCDMI method on 80:20. Figs. 4a-4b the confusion matrix with precise detection and classification of each class. Fig. 4c shows the PR examination, reflecting maximal outcome across every class. Fig. 4d demonstrates the ROC investigation, exhibiting efficacious results with higher values of ROC for separate class labels.

Table 2 and Fig. 5 present the skin cancer detection of HDLFET-ESCDMI methodology at 80:20. On 80% TRPHE, the proposed HDLFET-ESCDMI model attains average accuy of 99.07%, precn of 94.71%, sensy of 92.73%, specy of 99.46%, F1Score of 93.62%, and GMeasure of 93.67%. Similarly, on 20% TSPHE, the proposed HDLFET-ESCDMI model obtains average accuy of 99.06%, precn of 93.42%, sensy of 93.73%, specy of 99.47%, F1Score of 93.15%, and GMeasure of 93.36%.

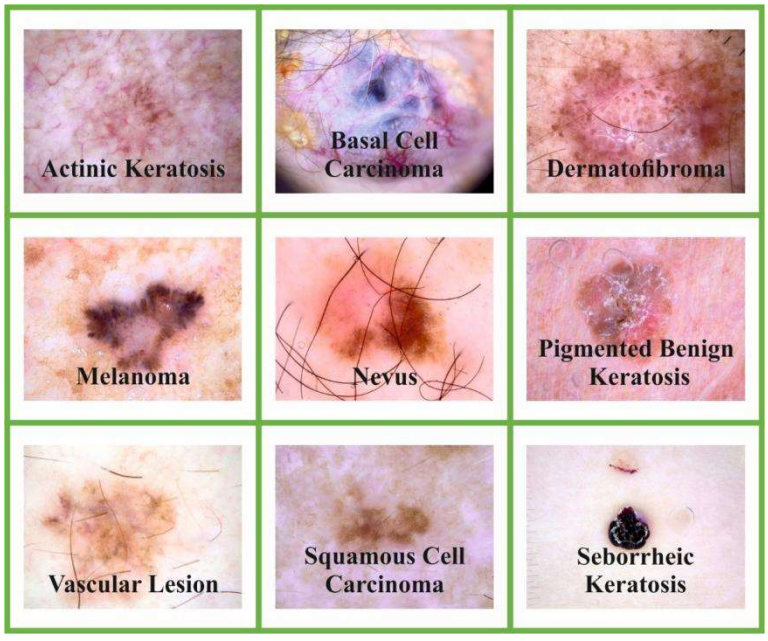

Figure 3: Sample Images

Table 1: Details of database

Diseases	Class Labels	Images
"Actinic Keratosis"	AKIEC	114
"Basal Cell Carcinoma"	BCC	376
"Dermatofibroma"	DF	95
"Melanoma"	MEL	438
"Nevus"	NV	357
"Pigmented Benign Keratosis"	PBKIEC	462
"Seborrheic Keratosis"	SKIEC	77
"Squamous Cell Carcinoma"	SCC	181
"Vascular Lesion"	VASC	139
	Total Images	**2239**

Table 2 Skin cancer detection of HDLFET-ESCDMI model under 80:20

Class Labels	$Accu_y$	$Prec_n$	$Sens_y$	$Spec_y$	$F1_{score}$	$G_{Measure}$
TRPHE (80%)						
AKIEC	99.11	91.09	92.93	99.47	92.00	92.00
BCC	98.88	95.90	97.23	99.20	96.56	96.57
DF	99.16	91.55	87.84	99.65	89.66	89.67
MEL	99.33	97.47	99.14	99.38	98.30	98.30
NV	99.05	96.67	97.64	99.33	97.15	97.15
PBKIEC	98.72	96.51	97.30	99.09	96.90	96.91
SKIEC	99.11	93.33	76.36	99.83	84.00	84.42
SCC	98.94	94.37	92.41	99.51	93.38	93.38
VASC	99.33	95.45	93.75	99.70	94.59	94.60
Average	99.07	94.71	92.73	99.46	93.62	93.67
TSPHE (20%)						
AKIEC	98.21	66.67	93.33	98.38	77.78	78.88
BCC	99.33	97.73	98.85	99.45	98.29	98.29
DF	98.88	90.00	85.71	99.53	87.80	87.83
MEL	99.11	97.73	97.73	99.44	97.73	97.73
NV	99.33	95.24	100.00	99.23	97.56	97.59
PBKIEC	98.44	98.85	93.48	99.72	96.09	96.13
SKIEC	98.88	100.00	77.27	100.00	87.18	87.90
SCC	99.33	94.59	97.22	99.51	95.89	95.90
VASC	100.00	100.00	100.00	100.00	100.00	100.00
Average	99.06	93.42	93.73	99.47	93.15	93.36

Fig. 6 exemplifies the training (TRAIN) $accu_y$ and validation (VALID) $accu_y$ of a HDLFET-ESCDMI approach at 80:20 over 25 epochs. At first, both TRAIN and VALID $accu_y$ rise quickly, representing efficient pattern learning from the data. Around the epoch**,** the VALID $accu_y$ slightly exceeds the training accuracy, signifying good generalization without over-fitting. As training advances, it reflects maximum performance and a minmum performance gap between TRAIN and VALID. The close alignment of both curves in training suggests that the approach is well-regularized and generalized. This shows the approach's stronger capability in learning and retaining valuable features across both seen and unseen data.

Journal of Theoretical and Applied Information Technology
31st August 2026. Vol.104. No.16

ISSN: 1992-8645 www.jatit.org E-ISSN: 1817-3195

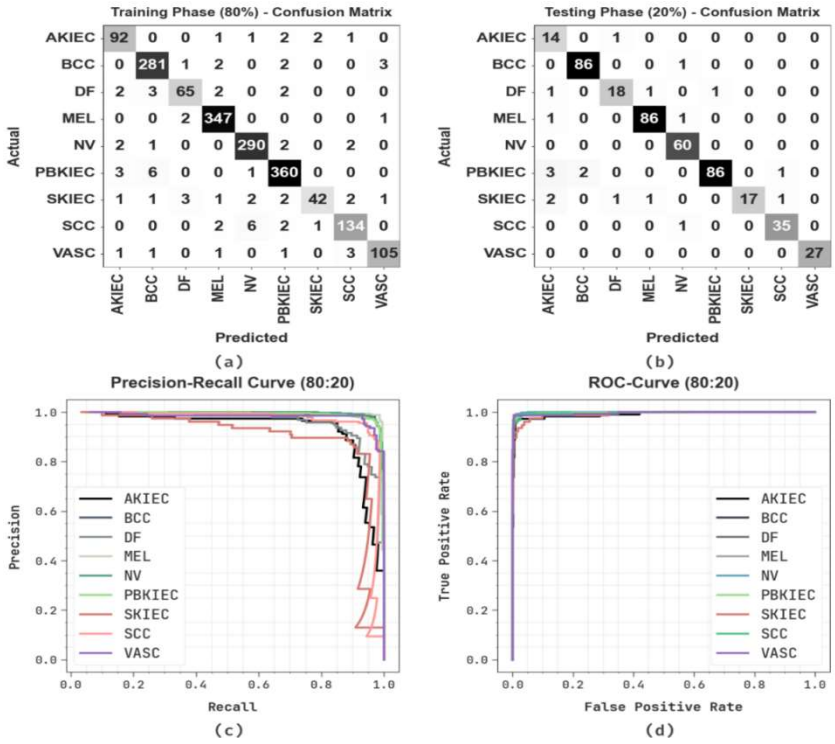

Figure 4: 80:20 (a-b) confusion matrices and (c-d) PR and ROC curves

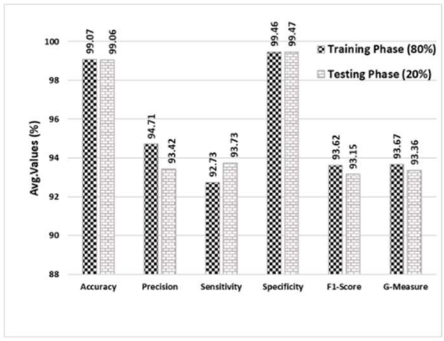

Fig. 5. Average value of HDLFET-ESCDMI model at 80%:20%

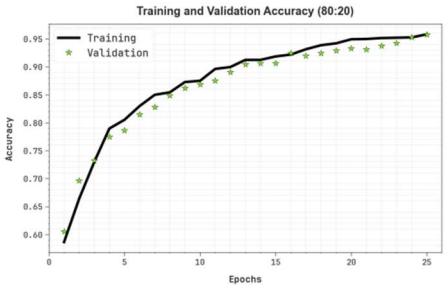

Fig. 6. Accu$_y$ curve of HDLFET-ESCDMI model at 80:20

Fig. 7 demonstrates the TRAIN and VALID losses of HDLFET-ESCDMI technique at 80:20 over 25 epochs. Initially, both TRAIN and VALID losses are higher, representing that the technique begins with partial understanding of the data. As training evolves, both losses steadily decline, displaying that the technique is efficiently

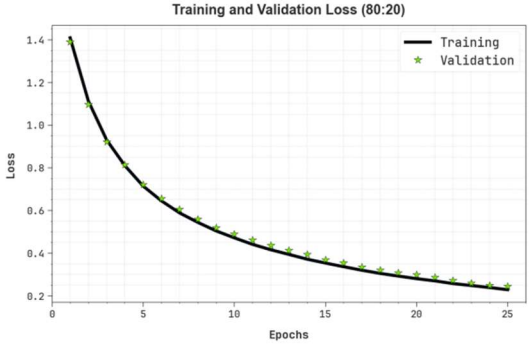

Fig. 7. Loss curve of HDLFET-ESCDMI method at 80:20

learning and enhancing its parameters. The close alignment between the TRAIN and VALID loss curves during training implies that the technique hasn't over-fitted and retains good generalization to unseen data. This steady and gradual decrease in loss reveals a stable, well-trained, and reliable deep learning model.

Fig. 8 characterizes the classifier outcomes of the HDLFET-ESCDMI methodology at 70:30. Figs. 8a-8b shows the confusion matrix with precise detection and classification of each class. Fig. 8c illustrate the examination of PR, specifying greater performance in every class. Ultimately, Fig. 8d portrays the ROC inspection, proving efficacious outcomes with elevated values of ROC for individual classes.

Table 3 and Fig. 9 demonstrate the skin cancer detection of HDLFET-ESCDMI algorithm on 70:30. At 70% TRPHE, the proposed HDLFET-ESCDMI model accomplishes average $accu_y$ of 99.06%, $prec_n$ of 95.24%, $sens_y$ of 92.64%, $spec_y$ of 99.46%, $F1_{Score}$ of 93.76%, and $G_{Measure}$ of 93.85%. Likewise, on 30% TSPHE, the proposed HDLFET-ESCDMI model achieves average $accu_y$ of 98.71%, $prec_n$ of 93.25%, $sens_y$ of 91.26%, $spec_y$ of 99.25%, $F1_{Score}$ of 92.15%, and $G_{Measure}$ of 92.20%.

Fig. 10 exemplifies the TRAIN $accu_y$ and VALID $accu_y$ of a HDLFET-ESCDMI model at 70:30 over 25 epochs. In the beginning, both TRAIN and VALID $accu_y$ increase fast, denoting effectual pattern learning from the data. Around the epoch, the VALID $accu_y$ surpasses the training accuracy slightly, implying good generalization without over-fitting. As training progresses, it reflects high performance and a low performance gap between TRAIN and VALID. The close alignment of both curves in training infers that the model is well-regularized and generalized. This reveals the model's stronger capability to learn and retain beneficial features across both seen and unseen data.

Table 3 Skin cancer detection of HDLFET-ESCDMI model under 70:30

Class Labels	$Accu_y$	$Prec_n$	$Sens_y$	$Spec_y$	$F1_{score}$	$G_{Measure}$
TRPHE (70%)						
AKIEC	99.43	96.15	92.59	99.80	94.34	94.36
BCC	98.92	95.44	98.05	99.08	96.72	96.73
DF	98.98	94.83	80.88	99.80	87.30	87.58
MEL	99.11	96.88	98.73	99.20	97.79	97.80
NV	98.79	96.75	95.58	99.39	96.16	96.16
PBKIEC	98.98	97.23	97.83	99.28	97.53	97.53
SKIEC	99.17	95.24	78.43	99.87	86.02	86.43
SCC	98.92	89.63	97.58	99.03	93.44	93.52
VASC	99.30	95.00	94.06	99.66	94.53	94.53
Average	**99.06**	**95.24**	**92.64**	**99.46**	**93.76**	**93.85**
TSPHE (30%)						
AKIEC	98.51	89.66	78.79	99.53	83.87	84.05
BCC	98.96	96.69	97.50	99.28	97.10	97.10
DF	99.11	88.89	88.89	99.53	88.89	88.89
MEL	98.07	91.73	98.39	97.99	94.94	95.00
NV	98.36	98.02	91.67	99.65	94.74	94.79
PBKIEC	98.66	95.77	97.84	98.87	96.80	96.80
SKIEC	99.40	95.83	88.46	99.85	92.00	92.07
SCC	98.36	88.33	92.98	98.86	90.60	90.63
VASC	98.96	94.29	86.84	99.68	90.41	90.49
Average	**98.71**	**93.25**	**91.26**	**99.25**	**92.15**	**92.20**

Method	$Accu_y$	$Prec_n$	$Sens_y$	$Spec_y$	$F1_{score}$
AttDenseNet-121	94.91	90.27	89.38	99.14	91.05
Inception-ResNetV2	98.05	92.28	90.90	90.22	92.06
PSOCNN	97.60	92.85	89.31	93.14	89.48
Wide-ShuffleNet	90.90	91.97	88.20	96.10	89.14
CRCKD Algorithm	97.26	88.89	91.07	92.33	90.69
Modified MobileNetV2	92.35	88.14	89.66	97.76	89.34
Modified DenseNet201	91.35	93.13	89.76	92.20	91.32
CNN+GoogLeNet	86.70	92.34	90.98	90.29	92.12
CNN+Fuzzy K-means	92.50	92.91	89.38	93.20	89.56
VGG16+ResNet+CapsNet	93.50	92.02	88.28	96.15	89.22
HDLFET-ESCDMI	99.07	94.71	92.73	99.46	93.62

Table 4 Comparative analysis of HDLFET-ESCDMI technique with recent models

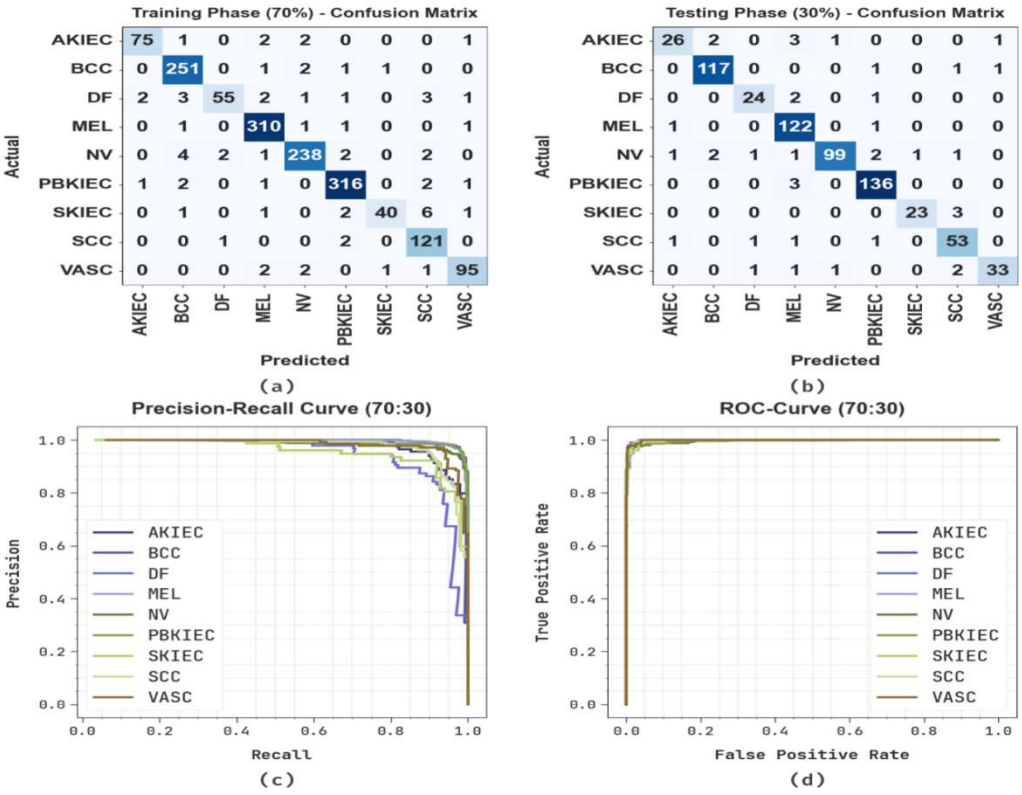

Fig. 8. 70:30 (a-b) confusion matrices and (c-d) PR and ROC curves

Fig. 11 exhibits the TRAIN and VALID losses of HDLFET-ESCDMI method at 70:30 over 25 epochs. Initially, both TRAIN and VALID losses are higher, showing the method begins with a partial understanding of the data. As training advances, both losses persistently reduce, demonstrating that the method is efficiently learning and optimizing its parameters. The close alignment between the TRAIN and VALID loss curves during training implies that the method hasn't over-fitted and upholds good generalization to unseen data. This persistent and steady decrease in loss indicates a reliable, well-trained, and stable deep learning model.

The comparative analysis of HDLFET-ESCDMI methodology with current models under various metrics is depicted in Table 4 [24-27].

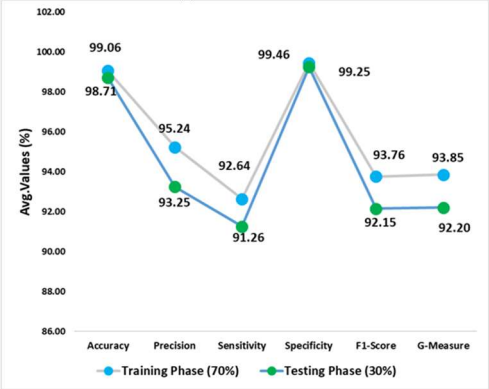

Fig. 9. Average values of HDLFET-ESCDMI model under 70:30

Fig. 10. $Accu_y$ curve of HDLFET-ESCDMI model under 70:30

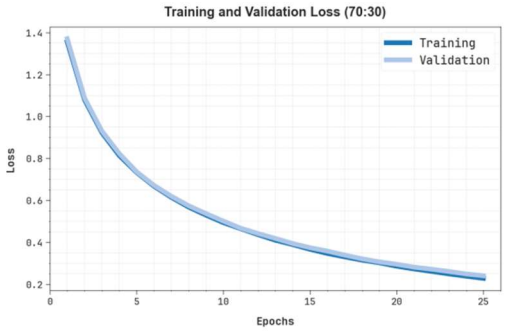

Fig. 11. Loss curve of HDLFET-ESCDMI model at 70:30

Fig. 12 presents simulation outcome of HDLFET-ESCDMI model with present methodologies at $accu_y$, $prec_n$, and $F1_{score}$. Based on $accu_y$, the HDLFET-ESCDMI system has the highest $accu_y$ of 99.07% whereas the AttDenseNet-121, Inception-ResNetV2, PSOCNN, Wide-ShuffleNet, CRCKD, Modified MobileNetV2, Modified DenseNet201, CNN+GoogLeNet, CNN+Fuzzy K-

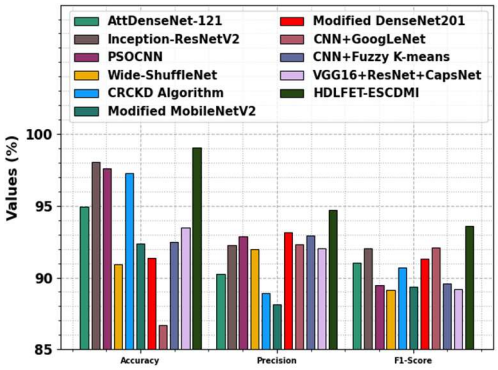

Fig. 12. $Accu_y$, $Prec_n$, and $F1_{score}$ outcome of HDLFET-ESCDMI model with existing techniques

means, and VGG16+ResNet+CapsNet approaches got lower $accu_y$ of 94.91%, 98.05%, 97.60%, 90.90%, 97.26%, 92.35%, 91.35%, 86.70%, 92.50%, and 93.50%, respectively. Similarly, on $F1_{score}$, the HDLFET-ESCDMI algorithm has the highest $F1_{score}$ of 93.62% while the AttDenseNet-121, Inception-ResNetV2, PSOCNN, Wide-ShuffleNet, CRCKD, Modified MobileNetV2, Modified DenseNet201, CNN+GoogLeNet, CNN+Fuzzy K-means, and VGG16+ResNet+CapsNet techniques have obtained lesser $F1_{score}$ of 91.05%, 92.06%, 89.48%, 89.14%, 90.69%, 89.34%, 91.32%, 92.12%, 89.56%, and 89.22%, respectively.

Fig. 13 illustrates $sens_y$ and $spec_y$ outcome of HDLFET-ESCDMI approach with existing models. Based on $sens_y$, the HDLFET-ESCDMI approach has obtained higher $sens_y$ of 92.73% while the AttDenseNet-121, Inception-ResNetV2, PSOCNN, Wide-ShuffleNet, CRCKD, Modified MobileNetV2, Modified DenseNet201, CNN+GoogLeNet, CNN+Fuzzy K-means, and VGG16+ResNet+CapsNet techniques have obtained lesser $sens_y$ of 89.38%, 90.90%, 89.31%, 88.20%, 91.07%, 89.66%, 89.76%, 90.98%, 89.38%, and 88.28%, correspondingly.

Also, based on $spec_y$, the HDLFET-ESCDMI approach has obtained higher $spec_y$ of 99.46% while the AttDenseNet-121, Inception-ResNetV2, PSOCNN, Wide-ShuffleNet, CRCKD, Modified MobileNetV2, Modified DenseNet201, CNN+GoogLeNet, CNN+Fuzzy K-means, and VGG16+ResNet+CapsNet techniques have obtained lesser $spec_y$ of 99.14%, 90.22%, 93.14%, 96.10%, 92.33%, 97.76%, 92.20%, 90.29%, 93.20%, and 96.15%, appropriately.

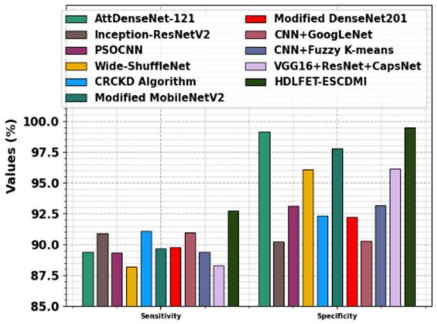

Fig. 13. $Sens_y$ and $Spec_y$outcome of HDLFET-ESCDMI approach with recent models

In Table 5 and Fig. 14, the time consuming (TC) of HDLFET-ESCDMI technique with current models is proven.

The proposed HDLFET-ESCDMI method offers a less value TC of 5.23% while the AttDenseNet-121, Inception-ResNetV2, PSOCNN, Wide-ShuffleNet, CRCKD, Modified MobileNetV2, Modified DenseNet201, CNN+GoogLeNet CNN+Fuzzy K-means, and VGG16+ResNet+CapsNet methodologies got the greatest TC of 21.41%, 23.52%, 15.34%, 17.00%, 10.73%, 11.69%, 8.21%, 9.00%, 13.11%, and 10.16%, respectively.

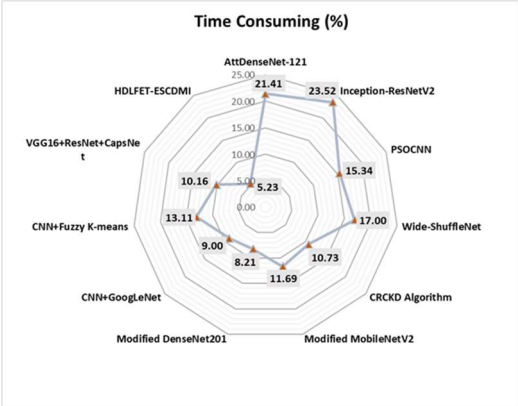

Fig. 14. TC outcome of HDLFET-ESCDMI model with recent methods

Table 5 TC outcome of HDLFET-ESCDMI model with recent methods

Method	Time Consuming (%)
AttDenseNet-121	21.41
Inception-ResNetV2	23.52
PSOCNN	15.34
Wide-ShuffleNet	17.00
CRCKD Algorithm	10.73
Modified MobileNetV2	11.69
Modified DenseNet201	8.21
CNN+GoogLeNet	9.00
CNN+Fuzzy K-means	13.11

4.1 Practical Implications

The proposed framework has several practical and industry-relevant benefits. First, its IoT-assisted design supports integration with dermatoscope-enabled handheld and wearable imaging devices, enabling remote and rural teledermatology screening where specialist dermatologists are scarce. Second, the model's low time consumption (5.23%, the lowest among compared methods) makes it suitable for near-real-time inference on cloud-connected or edge-assisted IoT healthcare platforms, supporting point-of-care decision support. Third, as a second-opinion CAD tool, the framework can reduce dermatologist workload and inter-observer variability in high-volume screening programs, while its consistently high specificity (>99%) limits false-positive referrals and associated healthcare costs. Fourth, the modular pipeline (pre-

processing, feature extraction, classification, tuning) can be embedded into existing mobile-health applications or hospital PACS/CAD software with minimal architectural change, offering a pathway for industry adoption by medical device and digital-health companies. Finally, the automated RBMO-based tuning reduces the engineering effort and domain expertise required to deploy and maintain such models, lowering the barrier to adoption in low-resource clinical settings.

5. CONCLUSION

This study presented HDLFET-ESCDMI, an IoT-assisted medical image analysis framework for accurate multi-class skin cancer diagnosis. The Ext-AFF technique suppressed speckle noise while preserving lesion boundaries; ConvNeXt-X extracted discriminative deep features by fusing convolutional and transformer-inspired design elements; a hybrid WGAN-AE model performed robust classification; and RBMO-based tuning optimized the classifier's hyperparameters. On the ISIC skin-cancer dataset (2,239 images, nine classes), the model achieved an average accuracy of 99.07%, precision of 94.71%, sensitivity of 92.73%, specificity of 99.46%, and F1-score of 93.62% under an 80:20 split, outperforming ten recent benchmark models while incurring the lowest time consumption (5.23%).

Notwithstanding these results, we note the following limitations. First, validation was performed on a single public dataset (ISIC); performance on multi-center data acquired from heterogeneous IoT imaging devices, different skin tones, and varying illumination conditions remains untested, which may affect generalizability. Second, minority classes such as Seborrheic Keratosis and Dermatofibroma consistently show lower sensitivity and precision than majority classes across all data splits, indicating that class imbalance is only partly mitigated. Third, the computational and memory cost of training the WGAN-AE component, and the added tuning overhead introduced by RBMO, were not benchmarked against simpler classifiers, so the accuracy gains should be weighed against training complexity. Fourth, the model currently operates as a “black box”; no explainability mechanism (e.g., Grad-CAM, SHAP) is provided to support clinical trust or dermatologist verification of predictions. Finally, real-time inference latency and energy consumption on constrained IoT edge devices, which are central to the paper's IoT framing, were not empirically measured. Future work will address multi-center and dermoscopy-device-diverse validation, lightweight/edge-optimized variants of ConvNeXt-X, integration of explainable-AI modules, and prospective clinical evaluation in collaboration with dermatologists.

6. OPEN ISSUES AND FUTURE DIRECTIONS

While HDLFET-ESCDMI achieved 99.07% accuracy and outperformed ten recent benchmark models, several open issues remain for future research:

Generalizability: Validation is limited to the single-source ISIC dataset; multi-center, multi-device, and multi-ethnicity dermoscopic datasets are needed to confirm robustness against device- and skin-tone-related variability.

Class imbalance: Minority classes (e.g., Seborrheic Keratosis, Dermatofibroma) show comparatively lower sensitivity/precision; more advanced imbalance-handling strategies (e.g., focal loss, targeted augmentation) warrant investigation.

Edge/real-time deployment: Inference latency, memory footprint, and energy consumption on resource-constrained IoT edge devices were not empirically benchmarked and are essential for real-world teledermatology deployment.

Explainability: The model currently lacks interpretability mechanisms (e.g., Grad-CAM, SHAP), which are important for clinical trust, regulatory approval, and dermatologist verification.

Computational cost: The added training complexity of the WGAN-AE and RBMO tuning stages relative to simpler classifiers has not been quantified and should be reported in future work.

Clinical validation: Prospective evaluation with dermatologists on real patient cohorts, alongside regulatory (e.g., medical-device) validation pathways, is required before clinical translation.

Multimodal fusion: Incorporating patient metadata (age, lesion history, anatomical site) alongside image data may further improve diagnostic accuracy and is left for future extension.

Data Availability Statement: The data supporting the findings of this study are openly available in the Kaggle repository at https://www.kaggle.com/datasets/nodoubttome/ski

n-cancer9-classesisic and are cited as Reference [23].

REFERENCES

[1] Tembhurne, J.V., Hebbar, N., Patil, H.Y. and Diwan, T., 2023. Skin cancer detection using ensemble of machine learning and deep learning techniques. Multimedia Tools and Applications, 82(18), pp.27501-27524.

[2] Dildar, M., Akram, S., Irfan, M., Khan, H.U., Ramzan, M., Mahmood, A.R., Alsaiari, S.A., Saeed, A.H.M., Alraddadi, M.O. and Mahnashi, M.H., 2021. Skin cancer detection: a review using deep learning techniques. International journal of environmental research and public health, 18(10), p.5479.

[3] Vijayalakshmi, M.M., 2019. Melanoma skin cancer detection using image processing and machine learning. International Journal of Trend in Scientific Research and Development (IJTSRD), 3(4), pp.780-784.

[4] Hasan, M., Barman, S.D., Islam, S. and Reza, A.W., 2019, April. Skin cancer detection using convolutional neural network. In Proceedings of the 2019 5th international conference on computing and artificial intelligence (pp. 254-258).

[5] Ameri, A., 2020. A deep learning approach to skin cancer detection in dermoscopy images. Journal of biomedical physics & engineering, 10(6), p.801.

[6] Monika, M.K., Vignesh, N.A., Kumari, C.U., Kumar, M.N.V.S.S. and Lydia, E.L., 2020. Skin cancer detection and classification using machine learning. Materials Today: Proceedings, 33, pp.4266-4270.

[7] Daghrir, J., Tlig, L., Bouchouicha, M. and Sayadi, M., 2020, September. Melanoma skin cancer detection using deep learning and classical machine learning techniques: A hybrid approach. In 2020 5th international conference on advanced technologies for signal and image processing (ATSIP) (pp. 1-5). IEEE.

[8] Nahata, H. and Singh, S.P., 2020. Deep learning solutions for skin cancer detection and diagnosis. Machine learning with health care perspective: machine learning and healthcare, pp.159-182.

[9] Roky, A.H., Islam, M.M., Ahasan, A.M.F., Mostaq, M.S., Mahmud, M.Z., Amin, M.N. and Mahmud, M.A., 2025. Overview of skin cancer types and prevalence rates across continents. Cancer pathogenesis and therapy, 3(02), pp.89-100.

[10] Abdelaziz, A. and Mahmoud, A.N., 2022. Skin Cancer Detection Using Deep Learning and Artificial Intelligence: Incorporated model of deep features fusion. Fusion: Practice and Applications, 8(2), pp.08-15.

[11] Sara, U., Das, U.K., Sikder, J. and Chowdhury, S.R., 2025. Automated Skin Cancer Classification and Detection Using Convolutional Neural Networks and Dermoscopy Images. Procedia Computer Science, 252, pp.108-117.

[12] Akinrinade, O. and Du, C., 2025. Skin cancer detection using deep machine learning techniques. Intelligence-Based Medicine, 11, p.100191.

[13] Kaur, R., GholamHosseini, H. and Lindén, M., 2025. Advanced Deep Learning Models for Melanoma Diagnosis in Computer-Aided Skin Cancer Detection. Sensors, 25(3), p.594.

[14] Kumar Lilhore, U., Simaiya, S., Sharma, Y.K., Kaswan, K.S., Rao, K.B., Rao, V.M., Baliyan, A., Bijalwan, A. and Alroobaea, R., 2024. A precise model for skin cancer diagnosis using hybrid U-Net and improved MobileNet-V3 with hyperparameters optimization. Scientific reports, 14(1), p.4299.

[15] Akilandasowmya, G., Nirmaladevi, G., Suganthi, S.U. and Aishwariya, A., 2024. Skin cancer diagnosis: Leveraging deep hidden features and ensemble classifiers for early detection and classification. Biomedical Signal Processing and Control, 88, p.105306.

[16] Asiri, Y., Halawani, H.T., Algarni, A.D. and Alanazi, A.A., 2023. IoT enabled healthcare environment using intelligent deep learning enabled skin lesion diagnosis model. Alexandria Engineering Journal, 78, pp.35-44.

[17] Reddy, N.R., Deshmukh, A.A., Rao, V.S., Godla, S.R., El-Ebiary, Y.A.B., Bravo, L.M.R. and Manikandan, R., 2023. Enhancing skin cancer detection through an AI-powered framework by integrating African vulture optimization with GAN-based Bi-LSTM architecture. International Journal of Advanced Computer Science and Applications, 14(9).

[18] Lai, W., Kuang, M., Wang, X., Ghafariasl, P., Sabzalian, M.H. and Lee, S., 2023. Skin cancer diagnosis (SCD) using artificial neural network (ANN) and improved gray wolf optimization (IGWO). Scientific Reports, 13(1), p.19377.

[19] Gupta, N., Kubicek, J., Penhaker, M. and Derawi, M., 2025. A novel diagnostic framework for breast cancer: Combining deep learning with mammogram-DBT feature fusion. Results in Engineering, 25, p.103836

[20] Talukder, M.A., 2025. A Hybrid Multiscale Feature Fusion Model For Enhanced Cardiovascular Arrhythmia Detection. Results in Engineering, p.104244.

[21] Alshehri, M.S., Saidani, O., Al Malwi, W., Asiri, F., Latif, S., Khattak, A.A. and Ahmad, J., 2025. A Hybrid Wasserstein GAN and Autoencoder Model for Robust Intrusion Detection in IoT. Computer Modeling in Engineering & Sciences.

[22] Zhu, C., Wang, Z., Peng, Y. and Xiao, W., 2025. An improved Red-billed blue magpie feature selection algorithm for medical data processing. PLoS One, 20(5), p.e0324866.

[23] https://www.kaggle.com/datasets/nodoubttome/skin-cancer9-classesisic

[24] Supriyanto, C., Salam, A., Zeniarja, J. and Wijaya, A., 2023. Two-stage input-space image augmentation and interpretable technique for accurate and explainable skin cancer diagnosis. Computation, 11(12), p.246.

[25] Alam, T.M., Shaukat, K., Khan, W.A., Hameed, I.A., Almuqren, L.A., Raza, M.A., Aslam, M. and Luo, S., 2022. An efficient deep learning-based skin cancer classifier for an imbalanced dataset. Diagnostics, 12(9), p.2115.

[26] Zia Ur Rehman, M., Ahmed, F., Alsuhibany, S.A., Jamal, S.S., Zulfiqar Ali, M. and Ahmad, J., 2022. Classification of skin cancer lesions using explainable deep learning. Sensors, 22(18), p.6915.

[27] Imran, A., Nasir, A., Bilal, M., Sun, G., Alzahrani, A. and Almuhaimeed, A., 2022. Skin cancer detection using combined decision of deep learners. ieee access, 10, pp.118198-118212.